Myeloid ALX/FPR2 regulates vascularization following tissue injury

Brian E. Sansbury[a], Xiaofeng Li[a], Blenda Wong[a], Andreas Patsalos[b,c], Nikolas Giannakis[d], Michael J. Zhang[e], Laszlo Nagy[b,c,d], and Matthew Spite[a,1]

[a]Center for Experimental Therapeutics and Reperfusion Injury, Department of Anesthesiology, Perioperative and Pain Medicine, Brigham and Women's Hospital and Harvard Medical School, Boston, MA 02115; [b]Department of Medicine, Johns Hopkins University School of Medicine and Johns Hopkins All Children's Hospital, St. Petersburg, FL 33701; [c]Department of Biological Chemistry, Johns Hopkins University School of Medicine and Johns Hopkins All Children's Hospital, St. Petersburg, FL 33701; [d]Department of Biochemistry and Molecular Biology, Faculty of Medicine, University of Debrecen, H-4032 Debrecen, Hungary; and [e]Department of Medicine, University of Minnesota Medical School, Minneapolis, MN 55455

Edited by Jason G. Cyster, University of California, San Francisco, CA, and approved May 6, 2020 (received for review October 16, 2019)

Ischemic injury initiates a sterile inflammatory response that ultimately participates in the repair and recovery of tissue perfusion. Macrophages are required for perfusion recovery during ischemia, in part because they produce growth factors that aid in vascular remodeling. The input signals governing this pro-revascularization phenotype remain of interest. Here we found that hindlimb ischemia increases levels of resolvin D1 (RvD1), an inflammation-resolving lipid mediator that targets macrophages via its receptor, ALX/FPR2. Exogenous RvD1 enhances perfusion recovery during ischemia, and mice deficient in *Alx/Fpr2* have an endogenous defect in this process. Mechanistically, RNA sequencing revealed that RvD1 induces a transcriptional program in macrophages characteristic of a pro-revascularization phenotype. Vascularization of ischemic skeletal muscle, as well as cutaneous wounds, is impaired in mice with myeloid-specific deficiency of *Alx/Fpr2*, and this is associated with altered expression of pro-revascularization genes in skeletal muscle and macrophages isolated from skeletal muscle. Collectively, these results uncover a role of ALX/FPR2 in revascularization that may be amenable to therapeutic targeting in diseases associated with altered tissue perfusion and repair.

macrophages | ischemia | resolvins

Impaired tissue perfusion is associated with peripheral artery disease and critical limb ischemia, diabetic wounds, and myocardial infarction, and can lead to necrosis, fibrosis, and loss of function (1, 2). Recovery from ischemic injury requires timely cessation of the inflammatory program and initiation of tissue restorative processes, including revascularization (3). Macrophages are active participants in both the inflammatory and reparative phases of the wound healing response (4–7). During the early phases of inflammation, macrophages produce proinflammatory mediators (e.g., cytokines, lipid mediators) and are programmed to assist in pathogen eradication. Macrophages are also key mediators of resolution of inflammation, involved in the clearance of apoptotic cells (i.e., efferocytosis) (8, 9). This process is associated with dampened proinflammatory mediator production and a transition to a tissue-reparative phenotype (4, 10). Indeed, macrophages are required for tissue revascularization during tissue injury, and they produce growth factors and cytokines that promote blood vessel growth and remodeling (11–13).

Resolution of inflammation is regulated in part by specialized proresolving lipid mediators (SPMs), such as resolvin D1 (RvD1) (14). The complete structure and stereochemical assignment of RvD1 (7*S*, 8*R*, 17*S*-trihydroxy-4*Z*, 9*E*, 11*E*, 13*Z*, 15*E*, 19*Z*-docosahexaenoic acid) was systematically elucidated (15, 16). RvD1 is produced by leukocytes and acts in an autocrine and paracrine manner to blunt neutrophil chemotaxis and proinflammatory cytokine production, as well as to enhance macrophage efferocytosis (14, 17, 18). These actions of RvD1 are mediated by specific G protein-coupled receptors, ALX/FPR2 and GPR32, in humans (18). In mice undergoing peritonitis, regulation of leukocyte trafficking by RvD1 is dependent on ALX/FPR2 (17, 19). In humans, vulnerable atherosclerotic plaques are deficient in RvD1 compared with stable plaques, and administration of RvD1 to mice with advanced atherosclerosis decreases necrotic cores and enhances macrophage efferocytosis (20). RvD1 also improves left ventricular function after myocardial infarction in mice (21) and reduces inflammation-driven neointimal hyperplasia following vein graft surgery (22).

While the RvD1-ALX/FPR2 axis has well-defined roles in macrophage efferocytosis and attenuation of proinflammatory cytokine production, whether this pathway engages macrophages to facilitate tissue repair during resolution is incompletely understood. Here we identified a role of the RvD1-ALX/FPR2 axis in regulating myeloid cell-dependent tissue revascularization during injury. These results highlight previously unrecognized roles of this pathway in the wound healing program that could potentially be amenable to therapeutic intervention.

Results

The RvD1-ALX/FPR2 Axis Plays a Causal Role in Revascularization during Ischemia. In response to ischemia, leukocytes are mobilized from the bone marrow and migrate to the injury site (6). Because leukocytes are both biosynthetic sources and cellular targets of resolvins that limit excessive inflammatory signaling

Significance

Ischemia is a major cause of morbidity and mortality and can lead to progressive tissue dysfunction. Ischemia promotes an inflammatory response that must be resolved to facilitate tissue repair and revascularization. Resolvins are lipid mediators that promote resolution of inflammation in part via specific receptors on macrophages. This study identifies that resolvin D1 is generated during tissue ischemia and induces a pro-revascularization phenotype in macrophages via its receptor, ALX/FPR2, leading to enhanced tissue perfusion. Because impaired resolution of inflammation in chronic inflammatory diseases is associated with altered tissue vascularization, these results could inform therapeutic approaches to improving tissue perfusion.

Author contributions: M.S. designed research; B.E.S., X.L., B.W., A.P., N.G., and M.J.Z. performed research; B.E.S., X.L., B.W., A.P., N.G., M.J.Z., L.N., and M.S. analyzed data; and B.E.S., L.N., and M.S. wrote the paper.

The authors declare no competing interest.

This article is a PNAS Direct Submission.

Data deposition: The RNA-seq data have been deposited in the Sequence Read Archive database (accession no. SRS4500032) and Gene Expression Omnibus (GEO) database, https://www.ncbi.nlm.nih.gov/geo (accession no. GSE128679).

[1]To whom correspondence may be addressed. Email: mspite@bwh.harvard.edu.

This article contains supporting information online at https://www.pnas.org/lookup/suppl/doi:10.1073/pnas.1918163117/-/DCSupplemental.

First published June 8, 2020.

and promote the resolution of inflammation (14), we assessed levels of RvD1 in mice undergoing hindlimb ischemia (HLI) by permanent femoral artery ligation. This surgical model induces sterile tissue injury and leads to endogenous perfusion recovery via revascularization in healthy mice (23). Using liquid chromatography-tandem mass spectrometry (LC-MS/MS), we found that RvD1 is increased as early as 24 h postsurgery, and that its levels were maintained for 3 d after surgery (Fig. 1 *A* and *B*). A representative MS/MS fragmentation spectrum of RvD1 from bone marrow is shown in Fig. 1*A*. Multiple studies have shown that macrophages are required for perfusion recovery in HLI (11–13). Because macrophages produce RvD1 (24), we hypothesized that RvD1 could also be produced in the ischemic muscle when macrophages accumulate in the injured tissue. Indeed, RvD1 was identified in skeletal muscle of the ischemic limb, and its levels were increased significantly over those seen in sham-operated mice by day 5 after induction of HLI (Fig. 1*B*).

The biological actions of RvD1 are mediated by ALX/FPR2 in mice (Fig. 1*C*). We observed a robust induction in *Alx/Fpr2* gene expression during ischemia in both bone marrow (>4-fold) and skeletal muscle (>21-fold) (Fig. 1*D*). To determine whether ALX/FPR2 is required for perfusion recovery, we performed HLI in mice with global deletion of *Alx/Fpr2*. We validated that *Alx/Fpr2* was expressed in wild-type (WT) macrophages and was absent in macrophages from *Alx/Fpr2*$^{-/-}$ mice (*SI Appendix*, Fig. S1 *A* and *B*). Using laser speckle contrast perfusion imaging, we observed that male WT mice recovered nearly 80% perfusion to the paw by day 10 post-HLI, while *Alx/Fpr2*$^{-/-}$ mice exhibited a sustained defect in perfusion recovery throughout the time course (Fig. 1*E*). This impaired perfusion was not observed in female *Alx/Fpr2*$^{-/-}$ mice (*SI Appendix*, Fig. S1*C*). RvD1 levels in skeletal muscle of male *Alx/Fpr2*$^{-/-}$ mice were slightly higher than those in WT mice on day 3 post-HLI and remained elevated at day 5 post-HLI (*SI Appendix*, Fig. S1*D*).

We next questioned whether perfusion recovery could be enhanced by exogenous delivery of RvD1, and whether this action is ALX/FPR2-dependent. When administered locally as a therapeutic agent beginning 24 h after HLI, RvD1 enhanced the already robust endogenous perfusion recovery in WT mice but had no effect in *Alx/Fpr2*$^{-/-}$ mice (Fig. 1*E*). Of note, systemic treatment with RvD1 (i.e., intraperitoneal [i.p.]) also enhanced perfusion recovery during HLI (*SI Appendix*, Fig. S2*A*). These results indicate that the RvD1-ALX/FPR2 signaling axis plays a causal role in revascularization after ischemia, and that the enhancement of perfusion recovery by therapeutically administered RvD1 is dependent on its receptor, ALX/FPR2.

Genetic Deficiency of *Alx/Fpr2* Impairs Neovascularization and Increases Tissue Fibrosis without Altering Macrophage Accumulation during HLI. Because *Alx/Fpr2*$^{-/-}$ mice have impaired perfusion recovery during HLI, we asked whether there were morphological and cellular changes occurring in the ischemic tissue associated with this defect. Immunofluorescence imaging of skeletal muscle at day 14 post-HLI revealed a significant decrease in the amount of CD31^{+} cells in *Alx/Fpr2*$^{-/-}$ mice compared with WT mice, consistent with altered neovascularization and impaired perfusion (Fig. 2*A*). Decreased perfusion and dysregulated inflammation commonly lead to exacerbated fibrosis (4). In addition, a separate study found that RvD1 decreases fibrosis in mice subjected to myocardial infarction, as defined by decreased expression of extracellular matrix regulatory genes leading to improved cardiac function (21). Therefore, we next evaluated the extent of fibrosis in *Alx/Fpr2*$^{-/-}$ mice by assessing collagen content in ischemic muscle. We found that expression of several collagens (e.g., *Col1a1, Col1a2, Col3a1, Col4a1*) was increased at day 5 post-HLI in *Alx/Fpr2*-deficient mice (Fig. 2*B*). By day 14, we observed a significant increase in collagen deposition, as assessed by picrosirius red staining, in *Alx/Fpr2*$^{-/-}$ mice compared with WT mice (Fig. 2*C*).

In other models of acute sterile inflammation, RvD1 reduces neutrophil recruitment via ALX/FPR2 (17, 19). Thus, we next asked whether differences in the tissue accumulation of neutrophils or macrophages could account for the impaired perfusion in *Alx/Fpr2*$^{-/-}$ mice. However, no differences in the percentage of neutrophils (CD45^{+}Ly6G^{+}F4/80^{-}) or macrophages (CD45^{+}Ly6G^{-}F4/80^{+}) were observed in the ischemic muscle of WT mice vs. *Alx/Fpr2*$^{-/-}$ mice at day 3 post-HLI (Fig. 2*D*). Moreover, local RvD1 treatment did not affect macrophage levels in ischemic muscle at day 3 post-HLI (*SI Appendix*, Fig. S2*B*). These data suggest that alterations in leukocyte recruitment are unlikely to explain the impaired perfusion observed in *Alx/Fpr2*$^{-/-}$ mice.

RvD1 Induces a Provascularization Phenotype in Macrophages. Macrophages are required for revascularization during HLI, and because macrophage accumulation was not altered in *Alx/Fpr2*-deficient mice with impaired tissue perfusion during HLI, we asked whether activation of this pathway regulates macrophage phenotype. To this end, we performed RNA sequencing (RNA-seq) (25, 26) analysis of naïve murine bone marrow-derived macrophages (BMDMs) stimulated with RvD1. This analysis revealed differential expression of 627 genes (353 up-regulated and 274 down-regulated) that met our inclusion criteria for normalized expression (≥3) and fold change (>1.5) in RvD1-stimulated macrophages relative to control.

To better understand and visualize the biological pathways associated with these gene changes, Gene Ontology (GO) enrichment analysis was performed in which related pathways are clustered into functionally grouped networks (Fig. 3*A*). As expected, RvD1-stimulated macrophages were enriched for genes involved in biological processes related to immunity and host defense, such as regulation of defense response, inflammatory response, innate immune response, and leukocyte chemotaxis. Surprisingly, an extensive network of 24 interrelated pathways associated with vascular development and regulation was also greatly enriched. Included in this vascular network were 9 of the 10 most significantly enriched pathways of the entire analysis (node size in Fig. 3*A* is correlated with statistical significance), indicating that RvD1 induces a vascular transcriptomic signature in macrophages.

Composing this broad vascular network are three specialized functional clusters of associated pathways (denoted by the purple, blue, and light-blue shading of the nodes in Fig. 3*A*). Here nodes with multiple colors have overlap in the genes represented in each pathway. To further define the identity of each cluster, we compiled all the genes that make up each of the 24 vascular process-related pathways and compared the degree of gene overlap of each cluster (Fig. 3*B*). A cassette of 34 genes (shown in the center of the Venn diagram; Fig. 3*B*) was common to all three clusters. Several of these genes encode receptors, ligands, and/or effectors of well-established mediators of vascular growth and remodeling. Specifically, members of the angiopoietin signaling family angiopoietin-1 receptor (*Tek*) and both *Angpt1* and *Angpt2* were identified, along with VEGF receptors 1 and 2 (*Flt1* and *Kdr*, respectively) and *Dll4*, a ligand of the Notch signaling family. We next quantified the ubiquity of the genes in this cassette among the 24 significantly enriched vascular process-related pathways. Here 21 of the 34 genes were found in ≥50% of vascular pathways, with *Tek*, *Kdr*, *Flt1*, and *Angpt1* the most common, found in ≥75% of vascular pathways (Fig. 3*C*).

Finally, we examined the RvD1-induced expression changes in all the genes contained in the vascular process-related pathways (Fig. 3 *D* and E). The majority of these genes were up-regulated by RvD1 (78 of 103, 76%), as were 28 of the cassette of 34 common genes from the cluster analysis (Fig. 3*D*). The expression

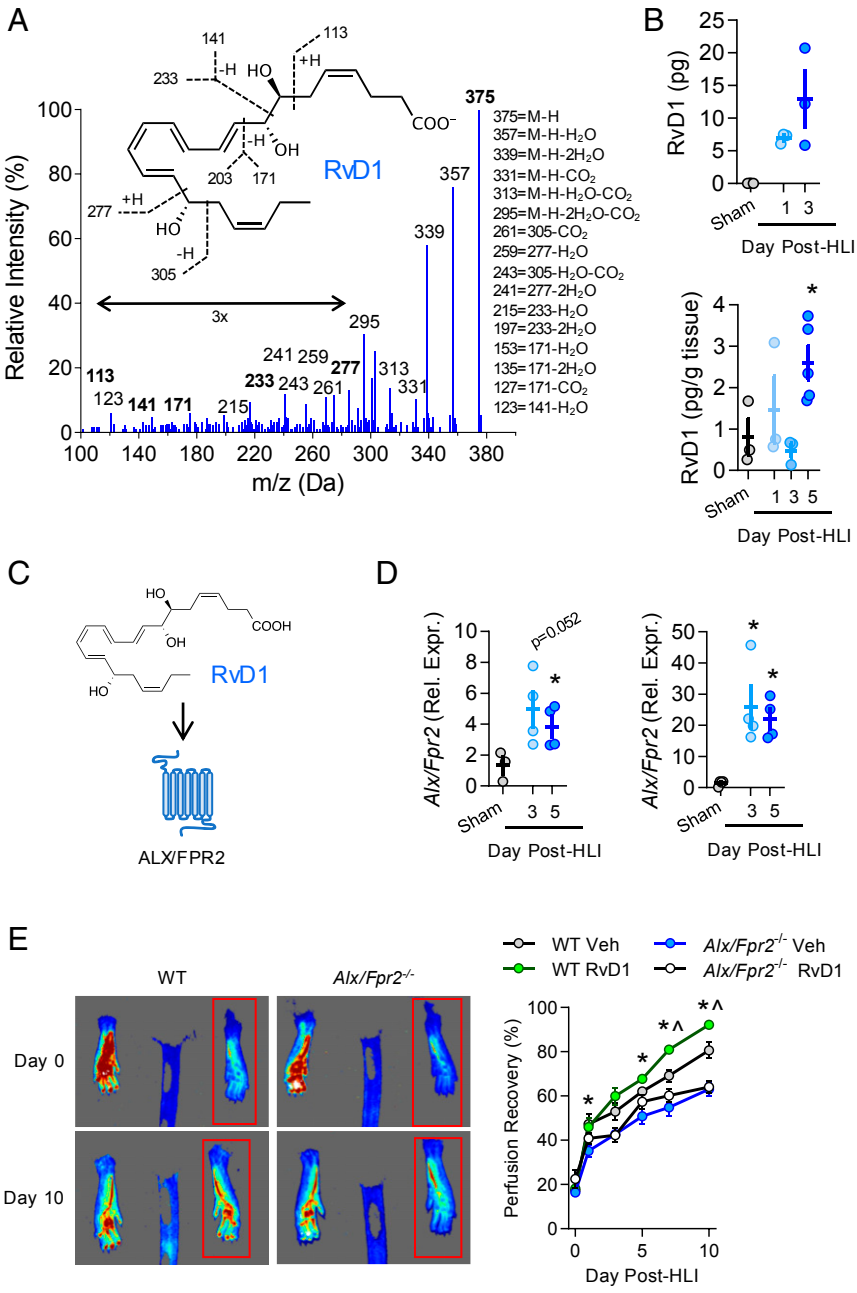

Fig. 1. The RvD1-ALX/FPR2 axis contributes to perfusion recovery during HLI. (*A*) Representative MS/MS fragmentation spectra of RvD1 identified in bone marrow of mice undergoing HLI (day 3). (*Inset*) Structure with diagnostic ion assignments. (*B*) Quantification of RvD1 in ischemic limb bone marrow (*Upper*) and skeletal muscle (*Lower*). $n = 3$ to 5 per group at each time point. (*C*) Schematic of RvD1 as a ligand for the ALX/FPR2 receptor. (*D*) Expression of *Alx/Fpr2* (relative to *Hprt*) in ischemic limb bone marrow (*Left*) and gastrocnemius muscle (*Right*) of mice undergoing HLI. $n = 4$ per group at each time point. In *B* and *D*, $*P < 0.05$ unpaired Student's *t* test vs. sham. (*E*) Representative laser speckle contrast perfusion images of vehicle-treated WT and *Alx/Fpr2*$^{-/-}$ mice shown on day 0 and day 10 of ischemia, with the red box indicating the ischemic limb. The graph shows quantification of perfusion recovery in WT and *Alx/Fpr2*$^{-/-}$ mice following HLI with daily administration of RvD1 (4 μg/kg s.c.) beginning at 24 h after surgery. $n = 6$ per group. Data represent mean ± SEM. $*P < 0.05$ WT vehicle vs. *Alx/Fpr2*$^{-/-}$ vehicle; $\wedge P < 0.05$ WT vehicle vs. WT RvD1, two-way ANOVA with Tukey's multiple comparison test.

changes observed in a subset of genes were further confirmed by qRT-PCR (*SI Appendix*, Fig. S3*A*).

As for the vascular pathways, we compiled all the genes in the immunity/host defense-related pathways and investigated the RvD1-induced expression changes (*SI Appendix*, Fig. S3 *B* and *C*). Several of the up-regulated genes are involved in the response to IFN signaling (e.g., *Rsad2*, *Usp18*, *Iigp1*), while others are critical for phagosome formation (e.g., *Lyst*). We note that some of the vascular-associated genes were also included in the immunity/host defense pathways. Taken together, these data indicate that RvD1 induces a transcriptomic signature in macrophages that is associated with tissue vascularization, as well as heightened immune functions, that are important for both host defense and tissue repair.

Myeloid-Specific Deficiency of *ALX/FPR2* Impairs Perfusion Recovery during HLI. After establishing that the revascularization program is defective in *Alx/Fpr2*$^{-/-}$ mice and that RvD1 induces a

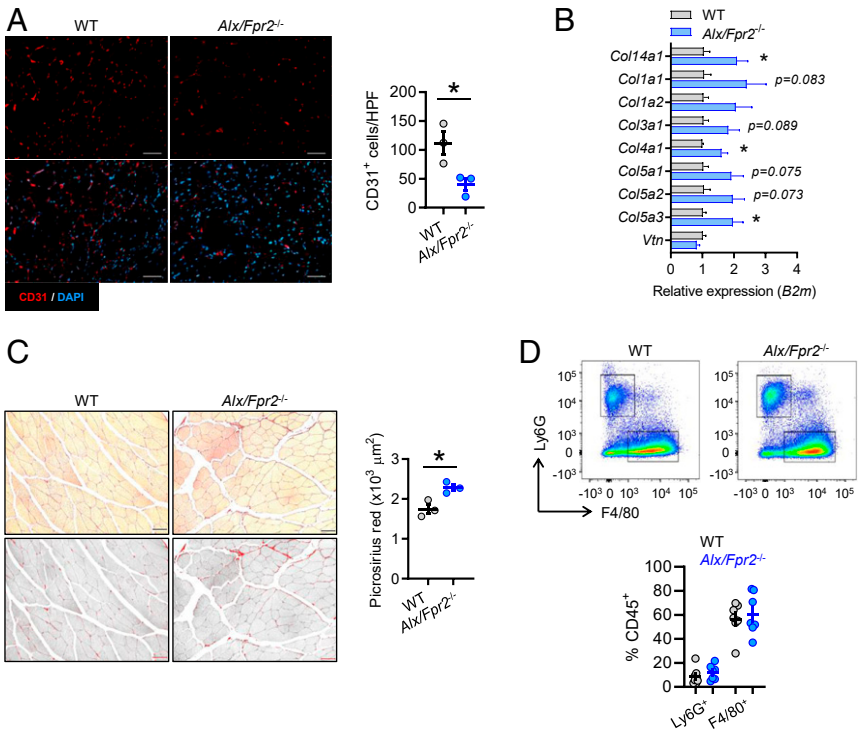

Fig. 2. Deficiency of *Alx/Fpr2* impairs ischemic limb neovascularization and induces fibrosis independently of changes in macrophage recruitment. (*A*) Representative immunofluorescence images and quantification of $CD31^+$ cells (per high-power field [HPF]) in ischemic gastrocnemius muscle of WT and *Alx/Fpr2*$^{-/-}$ mice on day 14 of HLI. $n = 3$ per group. (Scale bars: 50 μm.) (*B*) Gene expression of collagens (relative to *B2m*) in ischemic hamstring of WT and *Alx/Fpr2*$^{-/-}$ mice on day 5 of HLI. $n = 4$ per group. (*C*) Representative brightfield and grayscale images (*Left*) and quantification (*Right*) of picrosirius red-stained ischemic hamstrings of WT and *Alx/Fpr2*$^{-/-}$ mice on day 14 of HLI. (Scale bars: 50 μm.) $n = 3$ per group. (*D*, *Upper*) Representative flow cytometry dot plots of $CD45^+$ leukocytes isolated from ischemic gastrocnemius muscle on day 3 of HLI, with boxes indicating the $F4/80^+$ and $Ly6G^+$ populations. (*D*, *Lower*) Quantification of these populations. $n = 4$–7 per group. Data are presented as mean ± SEM. *$P < 0.05$, unpaired Student's *t* test.

provascular macrophage phenotype, we next questioned whether expression of ALX/FPR2 in myeloid cells is required for revascularization. For this, we generated mice with myeloid-specific deletion of *ALX/FPR2* by crossing humanized *ALX/FPR2-GFP* knockin floxed mice with mice expressing Cre recombinase under control of the lysozyme M promoter (LysM Cre) (Fig. 4*A* and *SI Appendix*, Fig. S4*A*). Loss of the GFP signal was validated by flow cytometry analysis in peripheral blood leukocytes of mice with myeloid-specific deficiency of *ALX/FPR2* (referred to as *hALX/FPR2*^{MKO}) (*SI Appendix*, Fig. S4*B*). Similar to the defect observed in global *Alx/Fpr2*$^{-/-}$ mice, we observed a significant impairment in perfusion recovery in male *hALX/FPR2*^{MKO} mice, which manifested by day 5 post-HLI and persisted through day 10 (Fig. 4*B*). A decreased abundance of $CD31^+$ cells in ischemic limb skeletal muscle of *hALX/FPR2*^{MKO} mice was also evident (Fig. 4*C*), consistent with mice with a global *Alx/Fpr2*-deficiency. No defect in perfusion recovery was observed in female *hALX/FPR2*^{MKO} mice compared with floxed controls (*SI Appendix*, Fig. S4*C*).

We next questioned the effect of myeloid-specific deletion of *ALX/FPR2* on expression of the vascular process-related genes that were up-regulated by RvD1 in BMDMs. We assembled a panel of RvD1-induced genes that were widely represented across the vascular development and remodeling pathways in the GO analysis (Fig. 3) and measured their expression in ischemic gastrocnemius muscle of *hALX/FPR2*^{MKO} mice (Fig. 4*D*). Several of these genes were down-regulated in *hALX/FPR2*^{MKO} mice compared with floxed mice, indicating that ALX/FPR2 expression in myeloid cells regulates their induction during HLI. Similar to what we observed in mice with global *Alx/Fpr2* deficiency, fibrosis was significantly increased in skeletal muscle of *hALX/FPR2*^{MKO} mice compared with floxed controls (Fig. 4*E*).

We have previously shown that RvD1 enhances tissue repair in skin wounds, and that mice globally deficient in *Alx/Fpr2* have an endogenous deficiency in wound reepithelialization (27). Thus, to determine whether the regulation of tissue vascularization that we observed during HLI extends to other tissue injury contexts, we assessed the vascularization of full-thickness cutaneous wounds excised from the dorsal skin of mice (5). Similar to what we observed in HLI, wound tissue of *hALX/FPR2*^{MKO} mice had a reduction in $CD31^+$ vessels compared with floxed mice, indicative of impaired vascularization during the early phase of tissue repair (day 3; Fig. 4*F*). Collectively, these results establish that activation of ALX/FPR2 signaling specifically in myeloid cells is required for optimal vascularization during tissue injury.

Myeloid-Specific Deficiency of *ALX/FPR2* Impairs Acquisition of a Provascularization Macrophage Phenotype. Because our results indicated that expression of *ALX/FPR2* in myeloid cells is required for perfusion recovery during HLI, we next questioned whether *hALX/FPR2*^{MKO} mice undergoing HLI have alterations in macrophage accumulation and phenotype in injured muscle. Consistent with our observations in the global *Alx/Fpr2*$^{-/-}$ mice, there were no differences in the accumulation of neutrophils ($CD45^+Ly6G^+F4/80^-$) or macrophages ($CD45^+Ly6G^-F4/80^+$) in the ischemic gastrocnemius muscles of *hALX/FPR2*^{MKO} mice at day 3 post-HLI compared with floxed mice (Fig. 5 *A* and *C*). To determine whether the phenotype of the macrophages was affected by loss of *Alx/Fpr2*, we first assessed the surface expression of Ly6C. We have previously shown that in a distinct

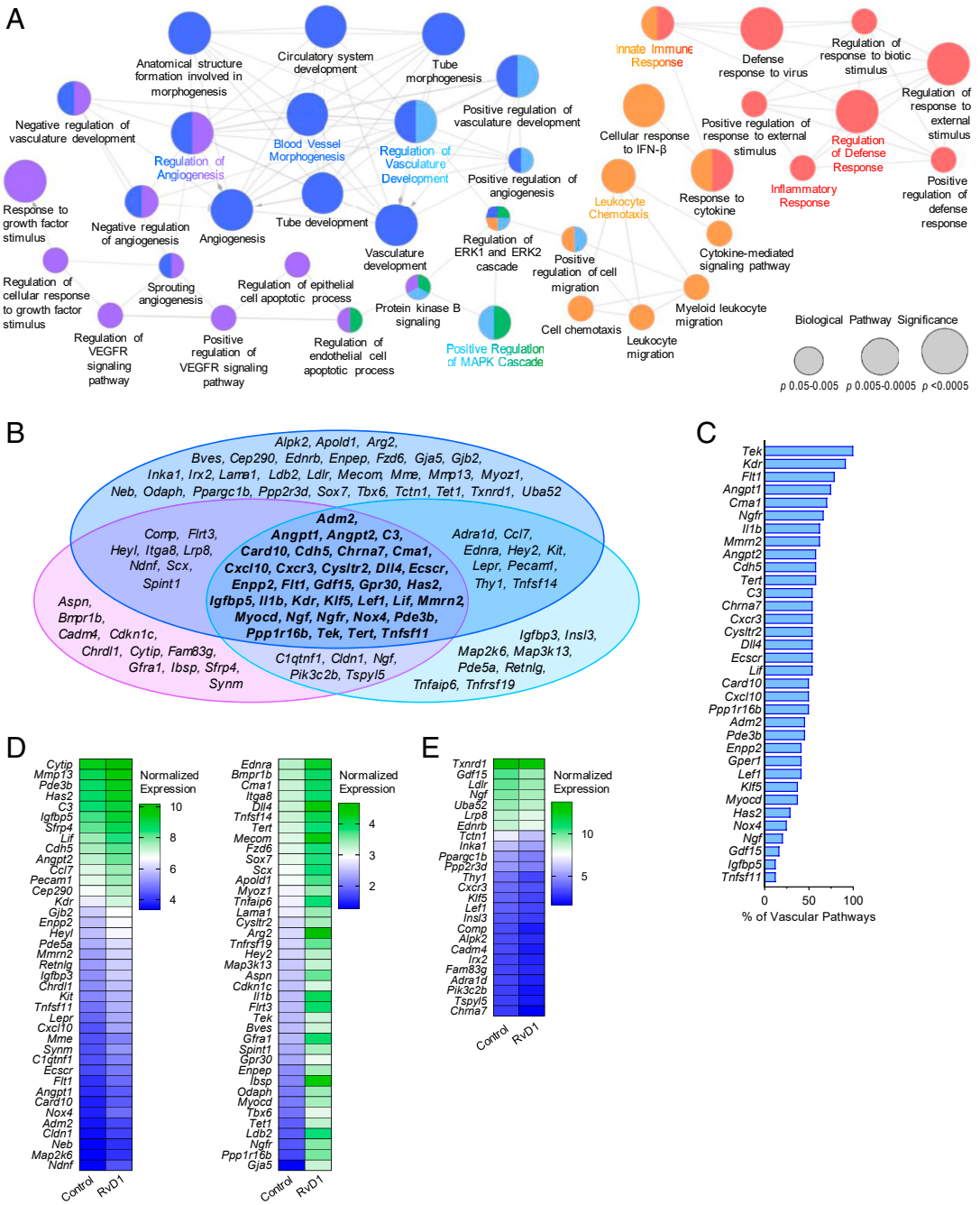

Fig. 3. RvD1 induces a provascular transcriptomic signature in macrophages. BMDMs isolated from WT mice were exposed to RvD1 for 6 h, then subjected to RNA-seq. (*A*) Graphical depiction of GO enrichment analysis of differentially expressed genes and their associated biological pathways. The colors of the nodes indicate functional clusters of related biological pathways (as determined by ≥50% gene overlap between pathways), and the node size is correlated with pathway enrichment significance. (*B*) Venn diagram displaying the component genes of the three vascular-related functional clusters. (*C*) Genes common to all three vascular-related functional clusters, listed by the percentage of all vascular process-related pathways in which that gene is associated. (*D* and *E*) RvD1-induced expression changes (*D*, up-regulated; *E*, down-regulated) in all genes contained in the vascular process-related pathways shown in heatmaps listed by decreasing normalized expression. $n = 3$ per group.

model of skeletal muscle injury and regeneration, exogenous delivery of another SPM, resolvin D2 (RvD2), triggers a shift from the proinflammatory Ly6C^{hi} to reparative Ly6C^{lo} macrophage populations (28). However, there were no differences in either the Ly6C^{hi} (CD45^{+}Ly6G^{-}F4/80^{+}) or Ly6C^{lo} (CD45^{+}Ly6G^{-}F4/80^{+}) macrophage subsets, and the ratio of these populations did not differ between *hALX/FPR2*^{MKO} mice and floxed mice at this time point (Fig. 5 *B* and *C*).

We next questioned whether the absence of *ALX/FPR2* impairs the ability of macrophages to adopt a provascularization phenotype. To this end, we isolated F4/80^{+} macrophages from ischemic gastrocnemius muscles on day 3 post-HLI and measured the expression of a panel of vascular-related genes that were induced by RvD1 in vitro (Fig. 5*D*). Consistent with our observation in the whole muscle tissue, several of the genes in this panel were down-regulated in macrophages isolated from

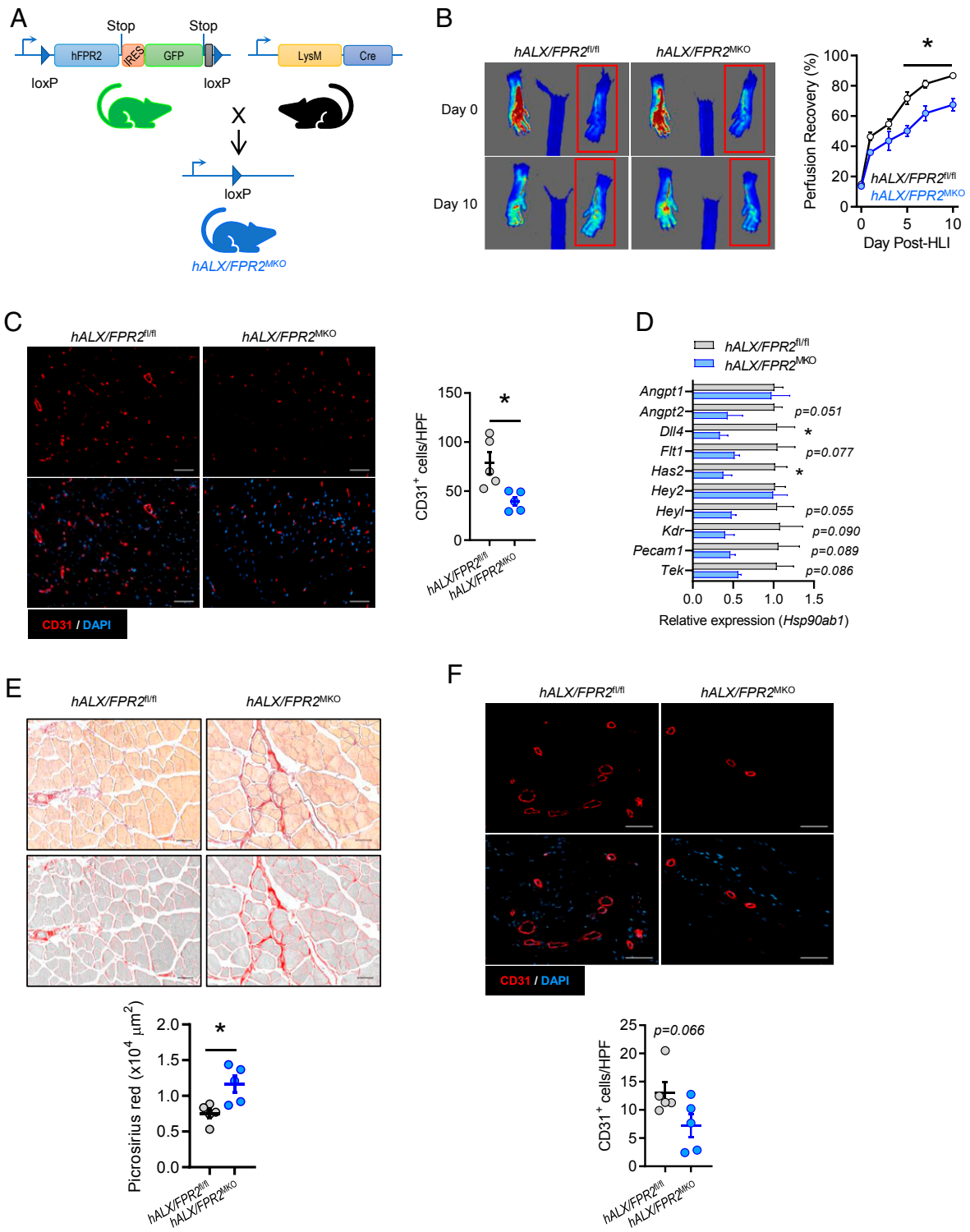

Fig. 4. Myeloid ALX/FPR2 has a cell-autonomous role in ischemic revascularization. (*A*) Schematic representation of the breeding strategy to generate myeloid-specific *ALX/FPR2* KO (*hALX/FPR2*^{MKO}) mice. The murine *Fpr2* gene was replaced with human *FPR2* (*hFPR2*) with a GFP reporter preceded by an internal ribosome entry site (IRES) to generate GFP^{+} *FPR2* floxed mice (*hFPR2*$^{fl/fl}$). These mice were then bred with *LysM-cre* mice to produce mice with myeloid-specific deletion of *FPR2* (*hALX/FPR2*^{MKO}). (*B*) Representative images (*Left*) and quantification (*Right*) of laser speckle contrast perfusion imaging in *hALX/FPR2*$^{fl/fl}$ and *hALX/FPR2*^{MKO} mice following HLI. The red box denotes the ischemic region of interest. $n = 8$ to 10 per group. *$P < 0.05$ at the indicated time points, two-way ANOVA with Sidak multiple comparison test of *hALX/FPR2*^{MKO} vs. *hALX/FPR2*$^{fl/fl}$. (*C*) Representative immunofluorescence images (*Left*) and quantification (*Right*) of CD31^{+} cells in ischemic gastrocnemius muscle of *hALX/FPR2*$^{fl/fl}$ and *hALX/FPR2*^{MKO} mice on day 14 of HLI. $n = 5$ per group. (*D*) Expression of vascular-related genes (relative to *Hsp90ab1*) in ischemic gastrocnemius muscle of *hALX/FPR2*$^{fl/fl}$ and *hALX/FPR2*^{MKO} mice on day 3 of HLI. $n = 3$ per group. (*E*) Representative brightfield and grayscale images (*Top*) and quantification (*Bottom*) of picrosirius red-stained ischemic hamstrings of WT and *Alx/Fpr2*^{MKO} mice on day 14 of HLI. $n = 5$ per group. (*F*) Representative immunofluorescence images (*Top*) and quantification (*Bottom*) of CD31^{+} cells in cutaneous wounds of *hALX/FPR2*$^{fl/fl}$ and *hALX/FPR2*^{MKO} mice on day 3 after wounding. $n = 5$ per group. Data are presented as mean ± SEM. In *C–F*, *$P < 0.05$, unpaired Student's *t* test. (Scale bars: 50 µm.)

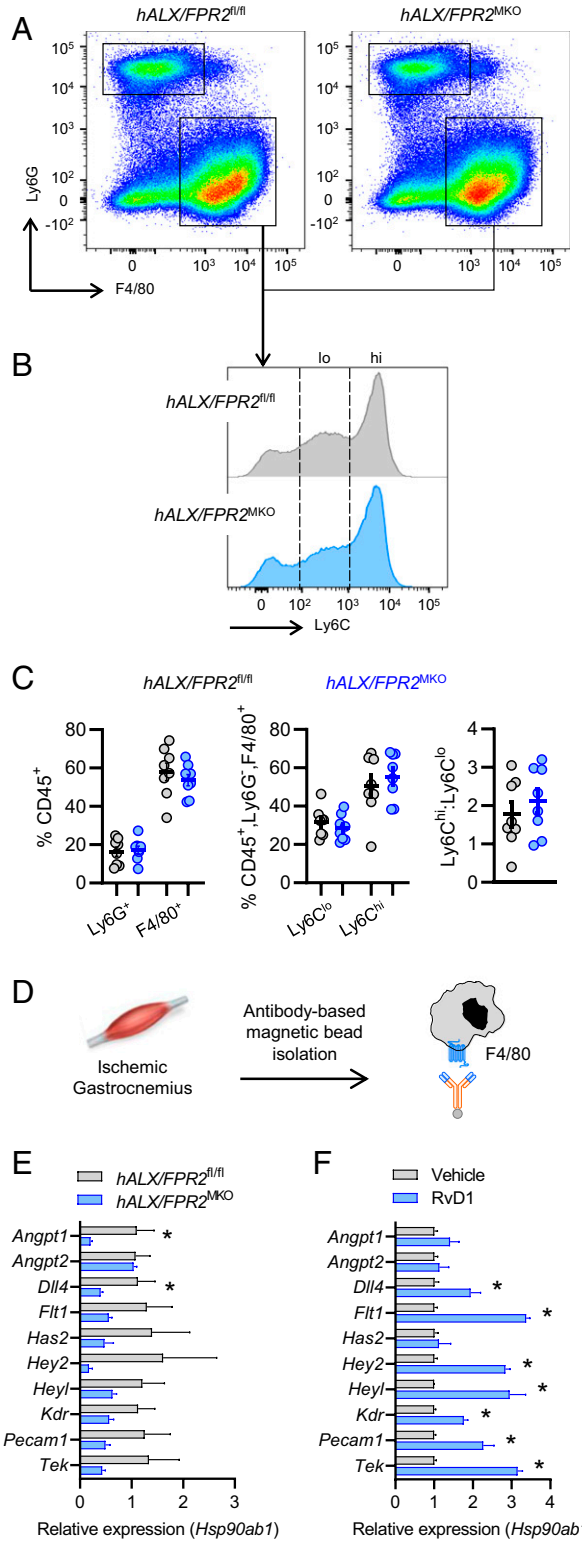

Fig. 5. Myeloid ALX/FPR2 promotes a provascular macrophage phenotype in response to ischemic injury. Ischemic gastrocnemius muscle from *hALX/FPR2*$^{fl/fl}$ and *hALX/FPR2*^{MKO} mice on day 3 of HLI were analyzed by flow cytometry. (*A*) Representative dot plots of CD45$^+$ leukocytes, with boxes indicating the F4/80$^+$ and Ly6G$^+$ populations. (*B*) Representative histograms of CD45$^+$F4/80$^+$ leukocytes, with dashed lines indicating the Ly6C^{lo} and Ly6C^{hi} populations. (*C*) Quantification of these populations and the ratio of Ly6C^{hi} cells to Ly6C^{lo} cells. $n = 8$ per group. (*D*) Schematic of F4/80$^+$ cell isolation from ischemic gastrocnemius muscle on day 3 of HLI. (*E* and *F*) Expression of vascular-related genes (relative to *Hsp90ab1*) in isolated F4/80$^+$ cells from *hALX/FPR2*$^{fl/fl}$ and *hALX/FPR2*^{MKO} mice (*E*) and WT mice (*F*) after daily administration of RvD1 (4 μg/kg s.c.). $n = 3$ to 4 per group. Data in graphs represent mean ± SEM. *$P < 0.05$, unpaired Student's *t* test.

ischemic muscle of *hALX/FPR2*^{MKO} mice compared with floxed mice (Fig. 5*E*). In contrast, RvD1 treatment of WT mice undergoing HLI increased expression of the majority of these genes in isolated macrophages (Fig. 5*F*). These results strongly suggest that ALX/FPR2 expression in macrophages is required for the adoption of a specific provascular transcriptomic signature that is critical for tissue repair after ischemic injury.

Discussion

The results of the present study demonstrate a role for RvD1 and its receptor, ALX/FPR2, in promoting tissue revascularization following ischemic injury. RvD1 induced a transcriptomic signature in macrophages suggestive of participation in tissue vascularization. Indeed, RvD1 was produced in ischemic tissue, and therapeutic administration of RvD1 enhanced perfusion recovery via ALX/FPR2. The endogenous role of this pathway in revascularization was demonstrated in mice with both global and myeloid-specific deficiency of *Alx/Fpr2*. These results indicate that the RvD1-ALX/FPR2 axis facilitates revascularization after ischemic injury largely through actions involving myeloid cells.

It is well documented that RvD1 stimulates resolution of inflammation in part by blunting excessive neutrophil recruitment and by promoting macrophage efferocytosis (15, 18, 19, 29). These proresolution actions of RvD1 are dependent on signaling through ALX/FPR2 in mice (17, 19). Here we observed that mice deficient in *Alx/Fpr2* have impaired revascularization and worsening of tissue fibrosis, suggesting an endogenous protective role of ALX/FPR2 in ischemic injury. These results are congruent with previous studies showing that mice deficient in *Alx/Fpr2* have increased inflammation associated with pneumonia (30), arthritis (31), and cerebral ischemia (32), as well as delayed tissue repair (i.e., reepithelialization) in skin wounds (27).

While it is known that ALX/FPR2 binds both proinflammatory and anti-inflammatory ligands (33), these previous studies, along with our present results, indicate that the presence of anti-inflammatory/proresolving ligands such as RvD1 bias the receptor to resolve inflammation and promote tissue repair (34). Along these lines, RvD1 mitigates tissue injury induced by ischemia and/or reperfusion in the heart, lungs, and liver (21, 29, 35, 36), although the cellular targets and effects on tissue vascularization in these contexts remain to be identified. We used laser speckle perfusion imaging to assess changes in tissue perfusion, as well as immunostaining for CD31 as a marker of vasculature. We cannot completely rule out the possibility that CD31 staining could also reflect changes in other cells, such as those in the lymphatic vasculature.

We observed a temporal regulation of RvD1 biosynthesis in the bone marrow during ischemia, with subsequent production in injured skeletal muscle. We speculate that leukocytes are the predominant cellular source of RvD1 in this context, although we cannot rule out the participation of other tissue resident cells. We have previously observed ischemia-induced increases in other resolvins in the bone marrow, such as RvD2 and RvD4 (37, 38), and found that isolated monocytes produce resolvins in a lipoxygenase-dependent manner (38). In addition, mice deficient in *Gpr18*, the specific receptor for RvD2, also have impaired recovery of perfusion during HLI, suggesting similar but nonredundant roles of RvD1 and RvD2 (38). These results extend previous findings in murine models of ischemia followed by reperfusion, in which D-series resolvins are biosynthesized and act as feedback regulators to blunt tissue damage (29, 37). Notably, levels of 15-epi lipoxin A_4, one of the first-identified

ligands of ALX/FPR2 (39, 40), are lower in individuals with intermittent claudication and critical limb ischemia compared with healthy individuals, suggesting potential dysregulation of this endogenous protective pathway in human limb vascularization (41). Previous studies have also revealed that resolvins can block certain forms of pathologic angiogenesis, such as that occurring in corneal neovascularization (42, 43). Thus, future studies are needed to fully understand how resolvins regulate the restoration of physiological tissue revascularization during wound healing while blocking pathological forms of inflammation-induced angiogenesis commonly associated with dysfunctional vasculature.

Several studies have demonstrated that RvD1 acts on macrophages to promote efferocytosis and to counter regulate proinflammatory signaling in a receptor-dependent manner (17, 18, 44). In addition, RvD1 enhances phagocytosis and dampens inflammatory cytokine production while stimulating production of anti-inflammatory cytokines in human primary macrophages (45, 46) and in adipose tissue macrophages of obese mice (44). In our unbiased transcriptome analysis, RvD1 induced expression of genes related to host defense (e.g., *Gbp3*, *C3*, *Rsad2*) but also those related tissue repair and revascularization, providing insight into the regulation of macrophage phenotype by RvD1. Several of these genes, such as *Dll4*, *Angpt2*, *Cxcl10*, and *Gpr30*, are necessary for restoration of revascularization during ischemia (47–50), indicating that RvD1 likely jumpstarts a tissue revascularization program rather than engaging a specific pathway. We confirmed that the RvD1-ALX/FPR2 axis regulates the expression of these genes in vivo using both gain-of-function (i.e., RvD1 treatment) and loss-of-function (i.e., *hALX/FPR2*^{MKO}) approaches. These changes in macrophage gene expression occurred independently of Ly6C surface expression. This is consistent with the transition from inflammation to tissue repair, in which macrophages respond to local cues and assume a spectrum of time-dependent phenotypes in both Ly6C^{hi} and Ly6C^{lo} macrophages (7).

While generally thought to be tissue-reparative and anti-fibrotic, prolonged activation or sustained recruitment of anti-inflammatory (or M2-like) macrophages may lead to fibrogenesis (4). We observed an increase in several fibrogenic genes and marked skeletal muscle fibrosis in *Alx/Fpr2*$^{-/-}$ mice after ischemia. Consistently, a separate study found that RvD1 decreases fibrosis in mice subjected to myocardial infarction (21). Thus, RvD1-ALX/FPR2 signaling induces a macrophage phenotype that promotes vascular remodeling and also potentially prevents excessive fibrogenesis allowing for accelerated tissue repair.

Overall, our present results assign a previously unrecognized function for ALX/FPR2 in the tissue revascularization program. These results suggest that agonism of ALX/FPR2 could potentially lead to new approaches to stimulating tissue repair in contexts associated with defective perfusion, such as peripheral artery disease, critical limb ischemia, and myocardial ischemia, as well as diabetic wounds. Because all of these conditions are similarly associated with chronic unresolved inflammation, targeting the RvD1-ALX/FPR2 axis could potentially provide distinct advantages over traditional anti-inflammatory approaches that could perturb tissue repair (10, 51–53).

Materials and Methods

Animals and Reagents. C57BL/6J (WT) mice and LysM-Cre (B6.129P2-Lyz2$^{tm1(cre)Ifo}$/J) mice were purchased from The Jackson Laboratory at 8 to 10 wk of age. Floxed human *ALX/FPR2-GFP* knockin mice (*hALX/FPR*$^{fl/fl}$) and *Alx/Fpr2*$^{-/-}$ mice were provided by Idorsia Pharmaceuticals. All animal procedures were approved by the Brigham and Women's Hospital Institutional Animal Care and Use Committee (#2016N000131). Animals were allocated to experimental groups at random, but investigators were not blinded to the identity of the groups. One mouse was excluded from the perfusion analysis due an adverse reaction to anesthesia. M-CSF was purchased from Sigma-Aldrich, and RvD1 was purchased from Cayman Chemical.

Surgical Procedures.

HLI model. Induction of HLI was performed as described previously (38). In brief, male and female C57BL/6J (WT), *Alx/Fpr2* KO (*Alx/Fpr2*$^{-/-}$), *ALX/FPR2* floxed (*hALX/FPR*$^{fl/fl}$), and *ALX/FPR2* myeloid-specific KO (*hALX/FPR2*^{MKO}) mice were anesthetized with 1.5% to 2% isoflurane (with O_2 at 2 L/min) and placed on a temperature-controlled water blanket to maintain a body temperature of 37 °C. After induction of anesthesia, hair was removed from the hindlimb using depilatory cream, and buprenorphine (0.5 mg/kg) was administered via subcutaneous (s.c.) injection. The mice were then placed in a supine position, and the paws were secured using surgical tape.

A small incision was made on the upper hind limb, just distal to the peritoneal ridge, perpendicular to the limb. The inguinal adipose tissue was gently separated with two pairs of forceps and moved away from the underlying tissue to expose the branching of the femoral and internal iliac arteries. Using ring forceps, the femoral artery and vein were carefully grasped and elevated, allowing two sutures to be passed underneath without damaging the vessels. These sutures were then used to create two ligatures of the vessels ~2 mm apart. The vessels were then transected between the ligatures using micro scissors, and the incision was closed using *n*-butyl-ester cyanoacrylate. For sham-operated animals, the incision was made, and sutures were passed under the vessels with no ligatures being tied.

Excisional cutaneous wound healing model. Full-thickness excisional cutaneous wounds were created as described previously (54). In brief, using depilatory cream, all hair was removed from the dorsal skin 1 d before wounding. The next day, *ALX/FPR2* floxed (*hALX/FPR*$^{fl/fl}$) and *ALX/FPR2* myeloid-specific KO (*hALX/FPR2*^{MKO}) mice were anesthetized with 1.5% to 2% isoflurane (with O_2 at 2 L/min) and placed on a temperature-controlled water blanket to maintain a body temperature of 37 °C. Buprenorphine (0.5 mg/kg) was administered via local s.c. injection. The mice were positioned on their side, and the dorsal skin was gently pulled away from the body, separating the skin from the underlying s.c. tissue.

Using a 5-mm biopsy punch, two full-thickness wounds were excised. Sterile saline (10 μL) was then added topically to each wound. Silicone splints were affixed to the skin surrounding the wounds with *n*-butyl-ester cyanoacrylate, and the wounds were covered with semipermeable polyurethane dressings. The injury site was then further protected by placing a self-adherent wrap around the animal covering the wounds. Each day, the wounds were exposed and sterile saline (10 μL) was added topically.

For both procedures, a second dose of buprenorphine (0.5 mg/kg) was administered via s.c. injection (either in the limb or on the back) at 24 h after surgery. In some HLI studies, RvD1 (4 μg/kg) in sterile saline (100 μL) or vehicle control was injected s.c. into the ligated limb or i.p. using an insulin syringe beginning 1 d after surgery. This administration was continued daily for up to 10 d after surgery. At the indicated day after surgery, the mice were killed by CO_2 inhalation, and cervical dislocation and tissues were collected for downstream analyses.

Targeted LC-MS/MS. The abundance of RvD1 was measured in the bone marrow and skeletal muscle (gastrocnemius and hamstring) of mice exposed to the sham procedure or HLI. Bone marrow and skeletal muscle from the ischemic limb were collected at the indicated days following HLI and placed in ice-cold methanol containing a deuterium-labeled RvD2 (d5-RvD2) synthetic standard. Bone marrow was immediately stored at −80 °C until further processing, while skeletal muscle tissue was minced on ice using scissors and then stored at −80 °C. The tissue was subjected to solid-phase extraction before to LC-MS/MS as detailed previously (55). In brief, samples were centrifuged (3,000 rpm for 10 min at 4 °C), and the supernatants were collected. Samples were then acidified (pH 3.5) before solid-phase extraction via C18 cartridges. Lipid mediators were eluted from the cartridge with methyl formate, and the solvent was evaporated under a constant gentle stream of N_2 gas. Samples were resuspended in methanol:water (50:50) and then analyzed by LC-MS/MS using a Poroshell reverse-phase C18 column (100 mm × 4.6 mm × 2.7 μm; Agilent Technologies)-equipped high- performance liquid chromatography (HPLC) system (Shimadzu) coupled to a QTrap 5500 mass spectrometer (AB Sciex). The QTrap was operated in negative ionization mode using scheduled multiple reaction monitoring (MRM) and specific transitions for RvD1 coupled with information-dependent acquisition (IDA) and enhanced product ion-scanning (EPI). RvD1 was identified using retention time and diagnostic MS/MS ions compared with an authentic standard (Cayman Chemical) and was quantified using MRM peak areas compared with an external standard curve generated with synthetic RvD1 and after normalization of extraction recovery based on the d5-RvD2 internal standard (Cayman Chemical).

Laser Speckle Contrast Perfusion Imaging. Immediately before surgical ligation and at the indicated time after surgery, perfusion to the hindlimbs was measured using a moorFLPI-2 full-field laser speckle imager and the moorFLPI-2 review software (Moor Instruments). Mice were anesthetized using isoflurane and maintained under 1.5% to 2% isoflurane (with O_2 at 2 L/min) on a heated water blanket at 37 °C while imaging was performed. To determine recovery, the perfusion in the ischemic limb was normalized to the nonischemic limb and expressed as percent recovery.

qRT-PCR. For analysis of fibrosis-related genes in ischemic limbs, hamstring muscles were collected from WT and *Alx/Fpr2*$^{-/-}$ mice at 5 d after surgical femoral artery ligation and stored in RNAlater solution (Qiagen) at 4 °C. To measure the expression of vascular-related genes, ischemic gastrocnemius muscle was removed at 3 d after ligation from *hALX/FPR2*$^{fl/fl}$ and *hALX/FPR2*^{MKO} mice or WT mice administered vehicle or RvD1 (4 μg/kg s.c.). The tissue was then either placed in RNAlater solution or subjected to single-cell isolation (details below). The muscle was disrupted using a glass pestle and homogenizer. RNA was isolated using RNeasy Mini Kit (Qiagen), and cDNA was synthesized using the Applied Biosystems High-Capacity cDNA Reverse Transcription Kit according to the manufacturer's instructions. qPCR was performed using SsoAdvanced Universal SYBR Green Supermix (Bio-Rad) on an Applied Biosystems QuantStudio 7 Flex real-time PCR system with PrimePCR assay primers (Bio-Rad) specific for *Col1a1*, *Col1a2*, *Col3a1*, *Col4a1*, *Col5a1*, *Col5a2*, *Col5a3*, and *Col14a1* for amplification. Primers for expression of *Alx/Fpr2*, *Angpt1*, *Angpt2*, *Dll4*, *Flt1*, *Gpr30*, *Has2*, *Hey2*, *Heyl*, *Hprt*, *Hsp90ab1*, *Kdr*, *Pecam1*, and *Tek* amplification were purchased from Qiagen and analyzed using the Bio-Rad CFX96 real-time PCR detection system.

For expression of collagens and vascular genes, data are presented as relative expression determined by the $2^{-\Delta\Delta CT}$ method after internal normalization to expression of *B2m* or *Hsp90ab1*, respectively. Expression levels of *Alx/Fpr2* and *Hprt* are shown as relative fluorescence units or as the mean cycle time required for signal amplification, as *Alx/Fpr2* was not detected in cells from *Alx/Fpr2*-deficient mice and thus could not be quantified using the $2^{-\Delta\Delta CT}$ method. Following PCR, the cDNA samples were subjected to electrophoresis using a 1% agarose gel stained with SYBR Safe DNA Gel Stain (APExBIO).

Immunofluorescence and Immunohistochemistry. To determine the extent of vascularization and fibrosis in injured tissue, ischemic muscle (gastrocnemius or hamstring) was collected on day 14 of HLI, and full-thickness cutaneous wounds were excised on day 3 after wounding and then fixed in formalin and embedded in paraffin. Cross- sections (5 μm) of the gastrocnemius muscle and wounds were cut and stained for CD31 (R&D Systems) with Cy3-conjugated donkey anti-goat IgG (Jackson ImmunoResearch) and DAPI (Invitrogen ProLong Diamond Antifade Mountant with DAPI). In gastrocnemius sections, CD31$^+$ cells were counted in 9 to 10 high-power fields in one tissue section from each animal. For wounds, CD31$^+$ cells were counted in 4 to 13 high-power fields from one bisected wound tissue section from each animal and averaged. For analysis of collagen deposition, cross-sections (5 μm) of the hamstring muscle were stained with picrosirius red (Millipore Sigma), and images were acquired at a magnification of 20×. The images were converted to grayscale using ImageJ, and a threshold was set for each image depending on the amount of background staining in each section. The area of positive staining was then calculated using the ImageJ measurement function. For quantification, a minimum of 4 fields and a maximum of 28 fields per tissue section were averaged for each animal.

Flow Cytometry and Cell Isolation. Leukocyte populations in ischemic gastrocnemius muscle were assessed via flow cytometry, and F4/80$^+$ cells were isolated on day 3 following surgical ligation. For this, WT (vehicle and RvD1-treated) and *Alx/Fpr2*$^{-/-}$ or *hALX/FPR2*$^{fl/fl}$ and *hALX/FPR2*^{MKO} mice were euthanized by CO_2 inhalation, cervical dislocation was performed, and the ischemic muscle was removed and subjected to a two-step digestion protocol (56). The tissue was first placed in a solution containing 75 U/mL collagenase II and 250 mM $CaCl_2$ in PBS and gently pulled apart using forceps, followed by incubation for 30 min at 37 °C. Following this incubation, the tissue was further physically disrupted using a syringe plunger, washed with cold PBS, then centrifuged (130 × *g* for 5 min at 4 °C). The tissue was resuspended in a second digestion solution containing 2.4 U/mL dispase II, 1.5 U/mL collagenase D, and 250 mM $CaCl_2$ in PBS, followed by incubation for 1 h at 37 °C, with low-speed vortex mixing at 15-min intervals. Digested tissue was finally filtered using a 40-μm cell strainer and washed in FACS buffer. The resulting suspension was spun down (515 × *g* for 5 min at 4 °C), resuspended in FACS buffer, and then subjected to analysis of leukocyte populations via flow cytometry or isolation of purified F4/80$^+$ cells. This was achieved using an F4/80 (APC anti-F4/80; eBioscience) antibody-based magnetic bead positive selection kit (EasySep; STEMCELL Technologies) according to the manufacturer's instructions. Expression of a panel of vascular-related genes was assessed in the purified cells as described above. For flow cytometry, cells were washed with FACS buffer, incubated in Fc-block, and stained with primary-conjugated fluorescent antibodies (PerCP anti-CD45, APC anti-F4/80, PE anti-Ly6G, and PE/Cy7 anti-Ly6C; eBioscience) for 30 min. For validation of myeloid-specific *ALX/FPR2* deletion, peripheral blood collected from mouse tails was incubated with lysis buffer to remove the red blood cells. After washing with FACS buffer, cells were analyzed based on GFP expression using a BD Biosciences FACSCanto flow cytometer and FlowJo software.

BMDM Isolation and Culture. Bone marrow was isolated from WT mice following euthanasia by CO_2 inhalation and cervical dislocation. The intact femurs and tibias from both legs were removed and cleaned of muscle tissue. The epiphyses of each bone were removed, and the bone marrow was flushed using a 25 G needle and 5 mL of basal medium (DMEM/F12, supplemented with 10 mM L-glutamine, 10% FBS, and 1% penicillin/streptomycin). Macrophages were differentiated in growth medium (basal medium supplemented with 10 ng/mL M-CSF or 20% L929 conditioned medium) as described elsewhere (57). On day 7 of differentiation, cells were liberated with a cell scraper, collected, and spun down at 400 × *g* for 10 min. Cells were then resuspended in basal medium, counted, and plated for experiments (six-well plates or 6-cm dishes). The following day, for RNA-seq and gene expression studies, cells were incubated without or with RvD1 (10 nM) in DMEM for 6 h, then lysed and collected in RLT buffer (Qiagen) containing 10 μL/mL β-mercaptoethanol and kept at −80 °C until RNA isolation.

RNA-Seq.

RNA isolation. RNA was isolated from macrophage samples using the RNeasy Mini Kit (Qiagen) according to the manufacturer's instructions.

RNA-seq library preparation. Using the TruSeq RNA Sample Preparation Kit (Illumina), a cDNA library was constructed from 100 to 400 ng of total RNA. This was achieved by pulling down poly-A-tailed RNA molecules with poly-T oligo-coated magnetic beads. The mRNA was then purified and fragmented with divalent cations at 85 °C, after which cDNA was synthesized with random primers and SuperScript II enzyme (Life Technologies). Next, second-strand synthesis was carried out, followed by end repair, single "A" base addition, and ligation of barcode indexed adaptors to the DNA fragments. PCR analyses specific to these adaptors were then performed to produce the sequencing libraries. Using E-Gel EX 2% agarose gels (Life Technologies), the libraries were size-selected and then purified with QIAquick Gel Extraction Kit (Qiagen), followed by sequencing with the Illumina HiSeq 2500 system.

RNA-seq analysis. For analysis, Tophat2 aligned the resulting reads to the mm10 mouse assembly, followed by downstream analysis of the aligned reads using StrandNGS version 2.8, build 230243. Once these steps were complete, the raw reads were normalized using the DESeq method and then subjected to statistical analyses. Genes with fold change >1.5 and $P < 0.05$, as determined by one-way ANOVA and Tukey's post hoc test on the normalized counts, were considered statistically significant and differentially expressed.

GO Enrichment Analysis. Genes meeting our inclusion criteria of normalized expression ≥3, fold change >1.5, and $P < 0.05$ were uploaded to the Cytoscape open source software platform, and GO analysis was performed using the ClueGO plug-in application (58). The resulting associated biological pathways/terms were then visually displayed in functionally grouped networks according to the similarity of the component genes within each term. To construct these networks, a two-tailed hypergeometric test was performed to test for enrichment and depletion within the dataset, followed by Bonferroni step-down correction for multiple testing of *P* values. Graphically, the size of the nodes reflects the significance associated with that term, while the color indicates the functionally grouped networks to which the term belongs. Nodes shaded with multiple colors indicate that ≥50% of the genes associated with that term are common to each of the functionally grouped networks indicated by the colors. All terms displayed met our inclusion criteria of a corrected *P* value of <0.05 and a minimum threshold of either three genes or 4% of all genes associated with the term were included on our list of RvD1-affected genes.

DNA Isolation and PCR for Mouse Genotyping. DNA was isolated from mouse tails by adding an alkaline digestion buffer (25 mM NaOH and 0.2 mM EDTA) and boiling the sample at 96 °C for 30 min. The digested samples were mixed with neutralization buffer (40 mM Tris·HCl), and the supernatants were subjected to PCR amplification with primers specific for the floxed human *FPR2* (forward, 5′- AGCCCAGAGTCCATTAGGCAGTACTCA-3′; reverse, 5′- CAG TGGAGAGATGTCAAAACCTTAATCAAAAA-3′) and/or the mouse LysM-*cre* (oIMR3066, 5′-CCCAGAAATGCCAGATTACG-3′; oIMR3067, 5′-CTTGGGCTG CCAGAATTTCTC-3′; oIMR3068, 5′-TTACAGTCGGCCAGGCTGAC-3′). The amplified products were then separated by electrophoresis using 1% agarose gels stained with SYBR Safe DNA Gel Stain (APExBIO).

Statistical Analysis. Data are presented as mean ± SEM. Statistical comparisons between two groups were conducted using an unpaired two-tailed Student's *t* test, while comparisons of multiple groups were performed using one-way ANOVA with Tukey's multiple comparison post hoc test. When assessing multiple groups over time, two-way ANOVA with Sidak's multiple comparison post hoc test was used. In all cases, a P value < 0.05 was considered to indicate statistical significance. GraphPad Prism 7.0 was used for all statistical analyses.

Data Availability. All the data generated in this study are included in the main text and *SI Appendix*. For the RNA-seq data reported here, the full dataset is publicly available from the Sequence Read Archive (accession no. SRS4500032) and the Gene Expression Omnibus database (accession no. GSE128679).

ACKNOWLEDGMENTS. Support for this work was provided by NIH Grants HL106173 (to M.S.), GM095467 (to M.S.; Project 3 and Core B), and DK115924 (to L.N.). B.E.S. is supported by an NIH National Research Service Award (HL136044).

1. M. H. Criqui, V. Aboyans, Epidemiology of peripheral artery disease. *Circ. Res.* **116**, 1509–1526 (2015).
2. P. Libby, G. K. Hansson, Inflammation and immunity in diseases of the arterial tree: Players and layers. *Circ. Res.* **116**, 307–311 (2015).
3. J. P. Cooke, D. W. Losordo, Modulating the vascular response to limb ischemia: Angiogenic and cell therapies. *Circ. Res.* **116**, 1561–1578 (2015).
4. S. A. Eming, T. A. Wynn, P. Martin, Inflammation and metabolism in tissue repair and regeneration. *Science* **356**, 1026–1030 (2017).
5. D. B. Gurevich *et al*., Live imaging of wound angiogenesis reveals macrophage-orchestrated vessel sprouting and regression. *EMBO J.* **37**, e97786 (2018).
6. F. K. Swirski, M. Nahrendorf, Leukocyte behavior in atherosclerosis, myocardial infarction, and heart failure. *Science* **339**, 161–166 (2013).
7. T. Varga *et al*., Highly dynamic transcriptional signature of distinct macrophage subsets during sterile inflammation, resolution, and tissue repair. *J. Immunol.* **196**, 4771–4782 (2016).
8. S. Morioka, C. Maueröder, K. S. Ravichandran, Living on the edge: Efferocytosis at the interface of homeostasis and pathology. *Immunity* **50**, 1149–1162 (2019).
9. C. N. Serhan *et al*., Resolution of inflammation: State of the art, definitions and terms. *FASEB J.* **21**, 325–332 (2007).
10. I. Tabas, C. K. Glass, Anti-inflammatory therapy in chronic disease: Challenges and opportunities. *Science* **339**, 166–172 (2013).
11. M. Heil *et al*., Collateral artery growth (arteriogenesis) after experimental arterial occlusion is impaired in mice lacking CC-chemokine receptor-2. *Circ. Res.* **94**, 671–677 (2004).
12. N. Jetten *et al*., Local delivery of polarized macrophages improves reperfusion recovery in a mouse hind limb ischemia model. *PLoS One* **8**, e68811 (2013).
13. G. Kuwahara, H. Nishinakamura, D. Kojima, T. Tashiro, S. Kodama, GM-CSF treated F4/80$^+$ BMCs improve murine hind limb ischemia similar to M-CSF differentiated macrophages. *PLoS One* **9**, e106987 (2014).
14. C. N. Serhan, B. D. Levy, Resolvins in inflammation: Emergence of the pro-resolving superfamily of mediators. *J. Clin. Invest.* **128**, 2657–2669 (2018).
15. Y. P. Sun *et al*., Resolvin D1 and its aspirin-triggered 17R epimer: Stereochemical assignments, anti-inflammatory properties, and enzymatic inactivation. *J. Biol. Chem.* **282**, 9323–9334 (2007).
16. C. N. Serhan *et al*., Resolvins: A family of bioactive products of omega-3 fatty acid transformation circuits initiated by aspirin treatment that counter proinflammation signals. *J. Exp. Med.* **196**, 1025–1037 (2002).
17. L. V. Norling, J. Dalli, R. J. Flower, C. N. Serhan, M. Perretti, Resolvin D1 limits polymorphonuclear leukocyte recruitment to inflammatory loci: Receptor-dependent actions. *Arterioscler. Thromb. Vasc. Biol.* **32**, 1970–1978 (2012).
18. S. Krishnamoorthy *et al*., Resolvin D1 binds human phagocytes with evidence for proresolving receptors. *Proc. Natl. Acad. Sci. U.S.A.* **107**, 1660–1665 (2010).
19. S. Krishnamoorthy, A. Recchiuti, N. Chiang, G. Fredman, C. N. Serhan, Resolvin D1 receptor stereoselectivity and regulation of inflammation and proresolving microRNAs. *Am. J. Pathol.* **180**, 2018–2027 (2012).
20. G. Fredman *et al*., An imbalance between specialized pro-resolving lipid mediators and pro-inflammatory leukotrienes promotes instability of atherosclerotic plaques. *Nat. Commun.* **7**, 12859 (2016).
21. V. Kain *et al*., Resolvin D1 activates the inflammation resolving response at splenic and ventricular site following myocardial infarction leading to improved ventricular function. *J. Mol. Cell. Cardiol.* **84**, 24–35 (2015).
22. B. Wu *et al*., Perivascular delivery of resolvin D1 inhibits neointimal hyperplasia in a rabbit vein graft model. *J. Vasc. Surg.* **68**, 188S–200S.e4 (2018).
23. A. Limbourg *et al*., Evaluation of postnatal arteriogenesis and angiogenesis in a mouse model of hind-limb ischemia. *Nat. Protoc.* **4**, 1737–1746 (2009).
24. J. Dalli, C. N. Serhan, Specific lipid mediator signatures of human phagocytes: Microparticles stimulate macrophage efferocytosis and pro-resolving mediators. *Blood* **120**, e60–e72 (2012).
25. B. E. Sansbury, N. Giannakis, A. Patsalos, M. Spite, L. Nagy, NCBI - GEO - Series GSE128679. Gene Expression Omnibus (GEO). https://www.ncbi.nlm.nih.gov/geo/query/acc.cgi?acc=GSE128679. Deposited 21 March 2019.
26. University of Debrecen, EMBL-EBI - Biosamples - SAMN1125797. EMBI-EBI - Biosamples. https://www.ebi.ac.uk/biosamples/samples?text=SRS4500032. Deposited 14 March 2019.
27. J. Hellmann *et al*., Biosynthesis of D-series resolvins in skin provides insights into their role in tissue repair. *J. Invest. Dermatol.* **138**, 2051–2060 (2018).
28. N. Giannakis *et al*., Dynamic changes to lipid mediators support transitions among macrophage subtypes during muscle regeneration. *Nat. Immunol.* **20**, 626–636 (2019).
29. K. Kasuga *et al*., Rapid appearance of resolvin precursors in inflammatory exudates: Novel mechanisms in resolution. *J. Immunol.* **181**, 8677–8687 (2008).
30. H. P. Sham *et al*., 15-epi-Lipoxin A_4, resolvin D2, and resolvin D3 induce NF-κB regulators in bacterial pneumonia. *J. Immunol.* **200**, 2757–2766 (2018).
31. L. V. Norling *et al*., Proresolving and cartilage-protective actions of resolvin D1 in inflammatory arthritis. *JCI Insight* **1**, e85922 (2016).
32. S. A. Vital *et al*., Formyl-peptide receptor 2/3/lipoxin A4 receptor regulates neutrophil-platelet aggregation and attenuates cerebral inflammation: Impact for therapy in cardiovascular disease. *Circulation* **133**, 2169–2179 (2016).
33. R. D. Ye *et al*., International Union of Basic and Clinical Pharmacology. LXXIII: Nomenclature for the formyl peptide receptor (FPR) family. *Pharmacol. Rev.* **61**, 119–161 (2009).
34. S. N. Cooray *et al*., Ligand-specific conformational change of the G-protein-coupled receptor ALX/FPR2 determines proresolving functional responses. *Proc. Natl. Acad. Sci. U.S.A.* **110**, 18232–18237 (2013).
35. K. Gilbert, J. Bernier, V. Bourque-Riel, M. Malick, G. Rousseau, Resolvin D1 reduces infarct size through a phosphoinositide 3-kinase/protein kinase B mechanism. *J. Cardiovasc. Pharmacol.* **66**, 72–79 (2015).
36. T. Zhang *et al*., Resolvin D1 protects against hepatic ischemia/reperfusion injury in rats. *Int. Immunopharmacol.* **28**, 322–327 (2015).
37. J. W. Winkler *et al*., Structural insights into Resolvin D4 actions and further metabolites via a new total organic synthesis and validation. *J. Leukoc. Biol.*, 10.1002/JLB.3MI0617-254R (2018).
38. M. J. Zhang *et al*., Resolvin D2 enhances postischemic revascularization while resolving inflammation. *Circulation* **134**, 666–680 (2016).
39. N. Chiang, I. M. Fierro, K. Gronert, C. N. Serhan, Activation of lipoxin A(4) receptors by aspirin-triggered lipoxins and select peptides evokes ligand-specific responses in inflammation. *J. Exp. Med.* **191**, 1197–1208 (2000).
40. S. Fiore, J. F. Maddox, H. D. Perez, C. N. Serhan, Identification of a human cDNA encoding a functional high-affinity lipoxin A4 receptor. *J. Exp. Med.* **180**, 253–260 (1994).
41. K. J. Ho *et al*., Aspirin-triggered lipoxin and resolvin E1 modulate vascular smooth muscle phenotype and correlate with peripheral atherosclerosis. *Am. J. Pathol.* **177**, 2116–2123 (2010).
42. K. M. Connor *et al*., Increased dietary intake of omega-3-polyunsaturated fatty acids reduces pathological retinal angiogenesis. *Nat. Med.* **13**, 868–873 (2007).
43. Y. Jin *et al*., Anti-angiogenesis effect of the novel anti-inflammatory and pro-resolving lipid mediators. *Invest. Ophthalmol. Vis. Sci.* **50**, 4743–4752 (2009).
44. E. Titos *et al*., Resolvin D1 and its precursor docosahexaenoic acid promote resolution of adipose tissue inflammation by eliciting macrophage polarization toward an M2-like phenotype. *J. Immunol.* **187**, 5408–5418 (2011).
45. A. Croasdell *et al*., Resolvins attenuate inflammation and promote resolution in cigarette smoke-exposed human macrophages. *Am. J. Physiol. Lung Cell. Mol. Physiol.* **309**, L888–L901 (2015).
46. Z. Gu *et al*., Resolvin D1, resolvin D2 and maresin 1 activate the GSK3β anti-inflammatory axis in TLR4-engaged human monocytes. *Innate Immun.* **22**, 186–195 (2016).
47. B. Cristofaro *et al*., Dll4-Notch signaling determines the formation of native arterial collateral networks and arterial function in mouse ischemia models. *Development* **140**, 1720–1729 (2013).

48. M. Lekas *et al*., Tie2-dependent neovascularization of the ischemic hindlimb is mediated by angiopoietin-2. *PLoS One* **7**, e43568 (2012).
49. P. van den Borne *et al*., Absence of chemokine (C-x-C motif) ligand 10 diminishes perfusion recovery after local arterial occlusion in mice. *Arterioscler. Thromb. Vasc. Biol.* **34**, 594–602 (2014).
50. B. R. Weil *et al*., Signaling via GPR30 protects the myocardium from ischemia/reperfusion injury. *Surgery* **148**, 436–443 (2010).
51. J. P. Cooke, Inflammation and its role in regeneration and repair. *Circ. Res.* **124**, 1166–1168 (2019).
52. C. Fowler, Do nonsteroidal anti-inflammatory drugs impair tissue healing? *JAAPA* **31**, 1–5 (2018).
53. A. B. Goldfine, S. E. Shoelson, Therapeutic approaches targeting inflammation for diabetes and associated cardiovascular risk. *J. Clin. Invest.* **127**, 83–93 (2017).
54. Y. Tang *et al*., Proresolution therapy for the treatment of delayed healing of diabetic wounds. *Diabetes* **62**, 618–627 (2013).
55. J. Dalli, R. A. Colas, M. E. Walker, C. N. Serhan, Lipid mediator metabolomics via LC-MS/MS profiling and analysis. *Methods Mol. Biol.* **1730**, 59–72 (2018).
56. R. N. Judson, M. Low, C. Eisner, F. M. Rossi, Isolation, culture, and differentiation of fibro/adipogenic progenitors (FAPs) from skeletal muscle. *Methods Mol. Biol.* **1668**, 93–103 (2017).
57. X. Zhang, R. Goncalves, D. M. Mosser, "The isolation and characterization of murine macrophages" in *Curr. Protoc. Immunol.*, (2008), Vol. Chapter 14, p. Unit 14 1.
58. G. Bindea *et al*., ClueGO: A Cytoscape plug-in to decipher functionally grouped gene ontology and pathway annotation networks. *Bioinformatics* **25**, 1091–1093 (2009).